Title	Three Dimensional Coupled Fluid-Droplet Model For Atmospheric Pressure Plasmas
Authors(s)	Iqbal, Muhammad M.; Stallard, Charlie P.; Dowling, Denis P.; Turner, Miles M.
Publication date	2014
Publication information	Plasma Processes and Polymers, 12 (3): 201-213
Publisher	Wiley
Item record/more information	http://hdl.handle.net/10197/5893
Publisher's statement	This is the author's version of the following article: Denis Dowling (2014) "Three Dimensional Coupled Fluid-Droplet Model For Atmospheric Pressure Plasmas" 12(3): 201-213 Plasma Processes and Polymers, which has been published in final form at http://dx.doi.org/10.1002/ppap.201400107.

Three Dimensional Coupled Fluid-Droplet Model For Atmospheric Pressure Plasmas

Muhammad M. Iqbal[1*], Charlie P. Stallard [2], Denis P. Dowling[2], Miles M. Turner[1*]

M. M. Iqbal, M. M. Turner
National Centre for Plasma Science and Technology, Dublin City University, Glasnevin, Dublin 9, Ireland. Email: muhammad.iqbal3@mail.dcu.ie

C. P. Stallard, D. P. Dowling
School of Mehcanical and Materials Engineering, University College Dublin, Belfield, Dublin 4, Ireland.

Abstract

A three-dimensional coupled fluid-droplet model is developed specifically to characterize the significance of droplet-plasma interaction at atmospheric pressure. The liquid droplet introduces a perturbation in atmospheric pressure plasma (APP) and under many conditions, the behavior of this perturbation is not clear during transport in PlasmaStream system. In this study, we identify the importance of ionization mechanism in two-phase flow. The affect and spatial expansion of vaporization in discharge plasma depend on the flow rate of liquid precursors. Penning ionization is recognized as the leading process along the pulse of evaporating droplets as compared to other ionization processes that explain the relevance of small nitrogen impurities in an APP. The influence of different precursors, such as Hexamethyldisiloxane, Tetraethyl orthosilicate and water is described by contrasting the implication of the evaporation process along the pulse of droplets in the APP. Finally, we validate the numerical simulation by comparison with the experimental observations of droplet size distributions using a laser diffraction particle size analysis technique as a part of atmospheric pressure plasma jet deposition system.

Keywords – atmospheric pressure plasma; droplet plasma modelling; two-phase flow; three-dimensional model;PlasmaStream System;

Introduction

In recent times, the functions of non-equilibrium atmospheric pressure plasmas are appreciated as an attractive and a promising source for numerous industrial and medical science applications, such as surface modification and etching of polymers [1], ozone generation [2], food processing [3], plasma-polymerized thin film [4], sterilization [5], coating of biomedical implants [6], cell detachment and tissue engineering [7] under several different operating conditions and chamber composition geometries. Generally, the behavior of a helium atmospheric pressure plasma is sharply modified by the presence of impurities in the form of gas, liquid and solid in which the interacting mechanism of solid and liquid phases is more complex than gas impurities, and which requires a detailed physical understanding of their phase transformations during interaction with plasma [8, 9] for diversified applications. In combustion applications, the technique for direct-injection of liquid precursors into gas mixture has been efficiently applied to achieve the desired output for the specific processes [10, 11] comprising of two-phase flow. The desired surface morphology of deposition coatings can be obtained by modulating monomer flow rates in atmospheric pressure plasma jets that discussed the behavior of various interesting mechanisms such as, saturation, nucleation and development of particulates in two-phase flow [12].

The introduction of specific amounts of precursor and gas flow rates have been recognized as the active controllers to obtain the required features of surface deposition, while the mechanism of interaction relies upon the chemical properties of gas mixture as well as liquid precursors [13, 14]. Fluid models are considered as satisfactory for the investigation of the physical phenomena involving stagnant and flowing plasmas, however, the data for the mobility and diffusivity of discharge species, excitation, ionization and other inelastic collision rate coefficients are calculated from the swarm experiments of concerned gas mixtures [15]. Perhaps, the accuracy of numerical simulations depends on several parameters, such as, mesh geometry, suitable algorithm and operating conditions, but the coherence

among them is essential to capture the effective outcomes for the specific experiment [16]. During the droplet-plasma interaction, the volumetric effect of external forces of the discharge plasma has significant impact on droplets during the transport in the channel of plasma stream [17]. The charging of droplets is perceived as an important factor to alter the characteristics of plasma deposition because of sheath formation around the droplets [18] and ultimately, it modifies the spatio-temporal density and energy distributions of plasma.

In this study, the complex interaction between the liquid precursor droplets and plasma are explored by the integration of a fluid and stochastic liquid droplet model in which the two models are working at different time scales, but the average values of electric field obtained from the plasma are passed down in the numerical solution of mass, momentum and energy equations for the liquid and gas phases. This produces a consistent updating of both models through the coupling source terms during the transport of two-phase flow. The realistic description of droplet-plasma interaction can be possible only by using a three-dimensional modelling approach because it explains in detail the precise aspects of liquid droplets during interaction with discharge species of plasma along the radial, axial and azimuthal directions. It is interesting to describe in detail the evolving conditions under which the phase shifting operation of liquid droplets transforms into vapours in case of various liquid precursors.

Experimental Plasma Chamber and Three Dimensional Coupled Fluid-Droplet Model

In this section, an explanation of PlasmaStream atmospheric pressure jet deposition system [19] and mathematical description of three-dimensional coupled fluid-droplet model are provided by illustrating their symbolic representations for two-phase flow. The various parts of experimental chamber are expressed by text labels in the schematic geometry of the chamber as shown in Figure 1.

Figure 1 (a) shows the symbolic representation of the PlasmaStream atmospheric pressure plasma jet deposition system with an additional arrangement of laser diffraction particle size analysis technique, which is used for the depositions of surface coating involving various types of precursors, such as HMDSO, TEOS and water. The axial length of a Polytetrafluoroethylene (PTFE) tube is measured as 75 mm long, while the inner diameter is evaluated as 15 mm. In the simulation domain, the oscillating sinusoidal potential ($V_0 \sin(2\pi ft)$) is applied to the thin metal electrode at a particular frequency (f) and the substrate is grounded. The laminar profiles of gas flow velocity are introduced at the inlet boundary of the chamber. At the upper portion (AB) of the chamber, a He-N_2 (99 % He and 1 % N_2) carrier gas flow is injected at two specific positions with gas flow rates (L/min) separated by a pin metal electrode as shown in Figure 1 (b), whereas the nebulizer droplets are inserted from the central location (B) with a flow rate (µL/min) interacting with APP. The radii (r_1, r_2, r_3 and R_0) represent the various boundaries of the chamber in the numerical model, which are implemented by using the approach of non-uniform meshing. The details of initial input parameters of the fluid - droplet model are described in Table 1.

For the liquid phase, it is handled by applying the Lagrangian method and an appropriate sample of droplets is introduced by utilizing x-squared distribution ($R(r_d) = \frac{r_d}{\bar{r}_d} e^{-\frac{r_d}{\bar{r}_d}}$), where r_d and $\bar{r}_d$ are the radius and mean radius of droplets. For the gas phase, the Eulerian approach provides adequate results for He-N_2 mixture. The Poisson's equation is solved numerically for the evaluation of electric potential by assuming an asymmetric electrode geometry of the chamber as shown in Figure 1 (b). The set of equations is applied to the modelling of plasma gas is

$$\left.\begin{aligned}
&\frac{\partial \rho_g}{\partial t_1} + \rho_g \vec{\nabla}.\vec{u}(r,\theta,z,t) = S \\
&\frac{\partial (\rho_g \vec{u}(r,\theta,z,t))}{\partial t_1} = \vec{\nabla} P + \vec{\nabla}.\vec{\Gamma}_\mu \nabla \vec{u}(r,\theta,z,t) + S_M \\
&\frac{\partial (\rho_g h)}{\partial t_1} = \vec{\nabla}.\frac{k}{C_p}\vec{\nabla} h + \vec{j}.\vec{E} + S_E \\
&\rho_g \frac{\partial Y}{\partial t_1} = \vec{\nabla}.D_{AB}\nabla Y + S
\end{aligned}\right\} \qquad (1 - 4)$$

Where the nomenclature of variables of the above set of equations is presented along with description in Table 4. The coupling source terms (S, S_M and S_E) bind two models, which are included in the fluid model equations of mass density, momentum and energy of APP and droplet in Eqs. (1 - 4). A stochastic liquid droplet model [20] is employed for the droplet-droplet mutual interactions, which involves the major collision interactions, such as grazing and coalescence of droplets. The Implicit Continuous Eulerian (ICE) method [21] is used in the present simulation study, which has been considered as decent and useful for the gas flows of any Mach number, and for the evaluation of terms involving a momentum exchange between two-phase flow. In case of plasma species, the kinetics of particles (e^-, He^+, He_2^+, N_2^+, He^* and He_2^*) are calculated by the numerical solution of the time-dependent continuity equation written as

$$\frac{\partial n_{sp}(r,\theta,z,t)}{\partial t_2} + \vec{\nabla}.\left(\vec{\Phi}_{sp}(r,\theta,z,t) + n_{sp}\vec{u}(r,\theta,z,t)\right) = S_{sp} \tag{5}$$

Where n_{sp}, $\vec{\Phi}_{sp}(r,\theta,z) = \text{sgn}(q_{sp})\mu_{sp}\vec{E}n_{sp} - D_{sp}\vec{\nabla}n_{sp}$ and S_{sp} represent the species density, drift-diffusion flux and source term for the production and annihilation of discharge species of distinctive chemical reactions described in [22] for He-N_2 gas mixture. The diffusion coefficient is evaluated by using the Einstein relation ($D_{sp} = \mu_{sp}k_BT_{sp}/q_{sp}$) for discharge species. The transport and reaction rate coefficients of electron impact chemical reactions are reliant on the electron mean energy, which are adjusted at every time step in the plasma model and operated as a strong coupling factor between the two-phase flow. The electron mean energy ($\bar{\varepsilon}$) is evaluated by using the electron energy density balance,

$$\frac{\partial n_{\varepsilon}(r,z,\theta,t)}{\partial t_2} + \vec{\nabla}.\left(\vec{\Phi}_{\varepsilon}(r,\theta,z,t) + \varepsilon n_{sp}\vec{u}(r,\theta,z,t)\right) = S_{\varepsilon} \tag{6}$$

Where $n_{\varepsilon}(r,\theta,z) = n_e(r,\theta,z)\,\bar{\varepsilon}(r,\theta,z), n_e$ is the electron density and $\vec{\Phi}_{\varepsilon}$ is the drift-diffusion flux in the electron energy density equation multiplying by a factor of 5/3. S_ε is the energy source term comprising of joule heating, electron energy losses and the implicit correction term, and the further

explanation of this term is available in [23]. The alternating direction implicit (ADI) solver [24] is used for the numerical solution of the particle balance equation of discharge species and electron energy density equations. In order to evaluate the electric field, the Poisson's equation is coupled with the plasma fluid model for the estimation of electric field ($\vec{\mathrm{E}}$), which is expressed as

$$\vec{\nabla}.(\varepsilon_0 \vec{\mathrm{E}}(r,\theta,z,t)) = -\sum_{\mathrm{sp}} q_{\mathrm{sp}} n_{\mathrm{sp}}(r,\theta,z,t) \tag{7}$$

Here ε_0 is the permittivity of the free space and the product ($q_{\mathrm{sp}}n_{\mathrm{sp}}$) represents the space charge density. So, the electric field strengths are calculated from the gradient of the electric potential along r, θ and z directions as $\mathrm{E}_r = -\frac{\partial V}{\partial r}$, $\mathrm{E}_\theta = -\frac{\partial V}{\partial \theta}$ and $\mathrm{E}_z = -\frac{\partial V}{\partial z}$. The numerical solution of Poisson's equation is obtained by applying successive over relaxation (SOR) method [25] in which the rapid convergence attains through the proper choice of overrelaxation parameter (ω) existing in the interval ($1.5 < \omega < 2$). The local field approximation implements to the ionic species in which the transport and reaction rate coefficients are expressed as the function of the electric field, and the effective electric field [26] is determined for the transport of ions. As the droplets drag in the plasma chamber, the rate of change of transient position (x_{p}), velocity (u_{p}), radius (r_{p}) and temperature (T_{p}) of droplets in the parcels are evaluated by the set of equations discussed in [10, 21].

Stochastic Liquid Droplet Model

A distinct x-squared distribution of droplets in various parcels is introduced from the central position in the computational grid along the radial, axial and azimuthal coordinate axes. The properties of droplets are identical in each parcel and the collisions only occur between different parcels. The collision frequency (ν_{c}) of a collector droplet with other droplets is determined by

$$\nu_{\mathrm{c}} = \frac{n_{\mathrm{p}_2}\pi(r_{\mathrm{col}} + r_{\mathrm{con}})^2 |u_{\mathrm{r}}|}{V_{\mathrm{ijk}}} \tag{8}$$

Where r_{col} and r_{con} are radii of the collector and contributor droplets respectively, $\vec{u}_r$ is the relative velocity of the two droplets in the parcels, n_{p_2} is the number of droplets in the particular parcel and V_{ijk} is the volume of the grid cell in which the interacting parcels are placed. The probability of missing collision can be revealed by the following formula as $P_0 = e^{-\bar{i}}$, where $\bar{i} = \nu_c \Delta t_1$, Δt_1 is the computational time step for the Lagrangian approach. The collision and critical impact parameters (b, b_{cr} respectively) are defined for the dynamics of droplets by the following relations as

$$\left.\begin{aligned} b &= (r_{col} + r_{con})\sqrt{Y} \\ b_{cr} &= (r_{col} + r_{con})\sqrt{E_{coal}} \end{aligned}\right\} \qquad (9 - 10)$$

Where E_{coal} is the coalescence efficiency and defined as $E_{coal} = \min(1.0, 2.4\zeta(\gamma)/W_e)$. The function $\xi(\gamma)$ is, for simplicity, approximated by [10] as $\xi(\gamma) = \gamma^3 - 2.4\,\gamma^2 - \gamma$ and $\gamma = r_{con}/r_{col}$. If $b \geq b_{cr}$, then the result of a collision is designated as grazing, such collisions appear strongly just after injection of droplet pulse. In case of grazing collision, the collectors and droplets in the parcels collide in such a way that they retain their radii and temperatures, but the velocities are altered after this interaction. If $b < b_{cr}$ the droplets coalesce to form a new droplet with greater radii during downward displacement in the plasma chamber. The values of constant parameters, such as molecular weight, specific heat of liquid and vapour phases, thermal conductivity, dynamic viscosity, latent heat of vaporization, mass density and surface tension of liquid precursors are collected from the source [27]. In coupled fluid-droplet model, several variables and constants are employed in the set of Eqs. (1 - 10), which are expressed in detail in Tables 1, 3 and 4.

Initial and Boundary Conditions

Here *u*, *v* and *w* are the axial, radial and swirl velocities of gas mixture. The axial velocity depends on the gas flow rates as explained in Table 2. For a solid pin electrode and a grounded substrate, the flux of the heavy charged particle species, electron, neutrals and electron energy density at the solid boundaries are computed by using the modified boundary conditions in [28, 29] during the alternate cycles of oscillating sinusoidal potential. We ignored the effect of secondary emission of electrons from the surface of electrodes in the present scenario because the ions have significantly small energy than electrons [30]. The average thermal velocities of the discharge species are evaluated using $v_{\mathrm{th,sp}} = \sqrt{8k_{\mathrm{B}}T_{\mathrm{sp}} / \pi m_{\mathrm{sp}}}$. The evaluation of electron mobilities as well as reaction rate coefficients of excitation and ionization processes are obtained by using Boltzmann solver (BOLSIG+) [31]. For the coupled model, the two different time steps (Δt_1, Δt_2) are used to control the two-phase flow in which the Courant–Friedrichs–Lewy (CFL) condition [15] $\Delta t_2 < \varepsilon_0 / \sum_p |q_p| \mu_p n_p$ is applied for the evaluation of the time step in case of discharge plasma, whereas the liquid and gas phases have a higher value of the time step (Δt_1) than the plasma time step (Δt_2) in this simulation study. The explanation of boundary conditions is provided in Table 2 for the fluid-droplet model.

Results and Discussion

Spatio-temporal Behavior of Droplet-Plasma Interaction

Low temperature APP, employed in the industrial processes is extremely complex while the numerical simulation modelling tools can provide an in-depth description of droplet-plasma interaction if the functioning conditions of the experiment implement precisely in the mathematical model. We consider several input operating parameters of the experiment [12] in three-dimensional fluid-droplet model to predict the complicated features of two-phase flow as shown in Table 4. In the first case, a pulse of water precursor droplets is introduced from the central location into the plasma chamber

existing in the size domain (2 μm ≤ r_d ≤ 13 μm) from the nebulizer. When the droplets interact with discharge plasma, they experience electrical ($\vec{E}$), aerodynamic drag ($\vec{F} = K_p(\vec{u} - \vec{u}' - \vec{u}_d) - (1/\rho_l)\vec{\nabla}p + \vec{g}_z$), internal viscous (μ_v) and gravitational ($\vec{g}$) forces during downward displacement in the PlasmaStream system containing He-N_2 discharge plasma. During interaction, the electrons and ions rush towards the surface of droplets, however, the droplets acquire negative potential on their surface due to greater mobility of electrons. The electrons around the water droplets perform an important role in the heating because of the non-equilibrium nature of discharge plasma in which the electrons and ions are present at two different temperatures. The electron mean energy lies approximately in the range of 0.1 eV - 5.0 eV, but the ionic species have similar temperature of gas mixture that is consistently updated from the evaluation of enthalpy of gas mixture as mentioned in Eq. (3). This means that the electrons are acting as a source of heat provider for the droplets and ultimately enhance the vaporization of droplets in discharge plasma. These interactive mechanisms will be tested by the application of various liquid droplets in order to describe the physical understanding between two-phase flow.

Figure 2 shows modelling results of the average temporal profiles of radius, temperature, axial velocity and vapour species density of water droplets during the interaction between the liquid and discharge plasma. It is seen from the distribution of mean radius that the rate of change of droplet radii is significantly smaller in the beginning, i.e., during the first 1 ms, and becomes expeditious as they attain the stationary state that is clearly verified from the mean profile of axial velocity of droplets as represented with a dash dotted blue line (c). The sharp decline in the mean radius of droplets provides a clear indication of strong evaporation in discharge plasma and it is confirmed from the increase in the temperature of water droplets in the parcels as illustrated by the green dotted line (b). Since the evaporation rate of droplets increases and its residue vapour represents another species called as vapour

species density as displayed by the black dashed line (d) in Figure 2. The vapour species density is calculated by the product of vapour species mass fraction (Y) and mass density of operating gas (ρ_g). This results as the enhancing of coupling between two phases during downward convection of liquid droplets in discharge plasma. The vapour species density increases until to steady-state just before the phase transformation of the entire pulse of droplets. During the downward drag, the local temperature of APP falls strongly in the surrounding volume of the droplet's pulse due to vaporization and it expands with the passage of time. The small spikes as shown with a pointed arrow in the profile of the mean radius of droplets in Figure 2 (for times greater than 7 ms) correspond to the rapid phase transformation of liquid droplets into vapours after obtaining the minimum radius due to the absorption of sufficient energy from the discharge plasma. After transformation of liquid droplet into vapour phase, the corresponding parcel is removed from the size distribution of droplets by modifying the entire size distribution of droplets afterwards. Therefore, the dynamic behavior of a droplet pulse in APP is clearly reflected from the mean profiles (a - d) of various parameters as shown in Figure 2 indicating the role of interaction between two-phase flow.

Influence of HMDSO Precursor Flow Rates

Because different kinds of liquid precursors are used for the treatment of surface depositions in the atmospheric pressure plasmas using the He-N_2 gas mixture, the effectiveness of HMDSO precursor droplets is analyzed by employing various flow rates of precursor existing in the domain (1 μm $\leq r_d \leq$ 6 μm) under similar constraints. The cone angle is considered as zero in the present simulation study and the pulse of liquid precursor is injected from the same location in each simulation. It is observed from the numerical simulations of HMDSO droplets that the duration of evaporation for the entire pulse of droplets is less than 1 ms in case of 10 μL/min, and this duration magnifies consecutively with an increment in the precursor flow rate for the considered distribution of droplets. Regarding the spatial expansion of the evaporation process in the radial, axial and azimuthal directions, it depends on the

amount of liquid precursor as shown clearly in the distribution of vapour species density in Figure 2. The entire pulse of liquid droplets is evaporated completely within the residence time of the gas mixture in the plasma chamber for the concerned flow rates of HMDSO precursors, while the radii of droplets exist in the nanometer domain just before the phase transformation of liquid precursors into vapours.

Figure 3 (a, b, c) illustrates the slice distributions of vapour species density at the specific locations of plasma chamber in order to elucidate the importance of vaporization of droplets under the above-mentioned precursor flow rates, such as at 10, 50 and 100 µL/min. As the HMDSO is volatile [12] in nature in He-N_2 APP, it evaporates so quickly forming a constricted carrier along the pulse of droplets. The channel of evaporation broadens continuously during the downward movement and it transfers its uniform ramification on the deposition of the substrate surface. It is observed from the spatial slice distributions that the effected volume in APP is amplified with an increment in the precursor flow rates from 10 to 100 µL/min as shown in Figure 3 (a - c) and resulted as the local cooling of gas near the vaporizing liquid droplets. The local cooling acts as a further impulse in the discharge plasma, which depresses the rate of evaporation near the present vaporizing droplets after obtaining the saturation condition. The temperature of the He-N_2 gas mixture is strongly modified by the impact of evaporation at different flow rates of precursors. This results as the reduction of gas temperature around the pulse of evaporating droplets. The appearance of local cooling is not highly probable at a small precursor flow rate ($\leq$ 10 µL/min), but it can become significant at higher precursor flow rates ($>$ 100 µL/min). Subsequently, the effect of higher precursor flow rate occurs as a wider spatial volume and magnitude of vapour species density than small flow rates as clearly shown in the slice distributions, which supports the development of the saturation condition in APP under higher precursor flow rate. This is verified by comparing the numerical values of vapour species density that amplifies from the lower to higher as (0.045×10^{-3}, 0.09×10^{-3} and 0.12×10^{-3} g/cm^3) along with 10, 50 and 100 µL/min. Therefore, the

higher amount of precursor flow rate exaggerates the cooling in APP and impedes the process of further evaporation during the downward flight of droplets.

Behavior of Penning Ionization

To explore the kinetics of charged particles during two-phase flow, the active behavior of discharge plasma is investigated by analyzing the ionization rates along the pulse of evaporating droplets in He-N_2 and He-Air gas mixtures. In He-N_2 gas, the Penning ionization is dominant due to involvement of molecular nitrogen participants, but in He-Air gas mixture, it is a combination of molecular nitrogen, atomic and molecular oxygen and water molecules. In the PlasmaStream system, the ionization is significantly stronger near the pin cathode and grounded substrate during the alternate peaks of discharge current pulse. The averaging of ionization rates for the entire chamber is not useful to explain the description of droplet-plasma interaction in the atmospheric pressure plasmas. Here, the averaging is performed by ignoring the volume near the cathode and grounded electrodes, which reflects the prominent aspects of interaction between the droplets and APP. Although, the nitrogen molecules (Penning impurities) have smaller ionization potential than helium atoms, but they strongly interact with metastables and generate ionization along the pulse of evaporating droplets and the same set of chemical reactions is employed in the present simulation study as discussed in [22]. We now compare the ionization rates produced by the influence of direct ionization (DI), Penning ionization (PI) and stepwise ionization (SI) in the bulk of APP.

Figure 4 contrasts the temporal profiles of ionization rates for the major mechanisms occurring in the bulk of APP with small gas impurities. It is clear from the values of various ionization rates that PI is recognized as extremely important during the discharge current pulses due to the expressive contribution of gas impurities at atmospheric pressure as represented with the black solid circle and plane solid lines

(a, a'). PI is dominant in He-air than He-N_2 gas mixture, which is appeared due to the effect of air as an impurity in APP in the former process. In He-N_2, the strong asymmetrical pattern of ionization rates is clearly observed from the plane lines (a', b', c'), but this asymmetry is reduced in case of He-Air gas mixture. This happens due to the effect of PI of multiple impurities enhancing the rate of evaporation along the pulse of droplets that shows the dynamic modifications in the sheath potential around the pulse of droplets. When the droplets are charged in the discharge plasma, the electrostatic attraction from the substrate sheath potential as well as gravitational pull strongly attracts the liquid droplets. This accelerates the droplets downward, but the magnitude of acceleration depends on the radii of droplets. It is seen from the numerical simulations that the higher radii of droplets (> 10 µL/min) are passed quickly from the plasma channel by partially contributing to the overall evaporation process. The SI mechanism is weaker than PI and DI processes as shown in Figure 4 (c, c') and it also performs an important role to destroy the metastables in order to maintain the stability of discharge plasma. Due to substantial impact of PI, the molecular nitrogen, atomic and molecular oxygen and water ions are prevalent along the pulse of droplets as compared to the atomic helium ions from DI as shown in Figure 4 (b, b'). The atomic helium ions from DI are immediately transferred to molecular helium ions through the channel of three body chemical reaction that are further converted into molecular nitrogen ions by using the path of charge transfer mechanism.

Near the pin cathode and grounded substrate, the DI performs an assertive role than PI and SI mechanisms, which is opposite to these mechanisms around the pulse of droplets as shown in Figure 4 (b, b'). This occurs by the primary contribution of small impurities in pure helium gas indicating in the gap spacing around the pulse of droplets at different flow rates as shown in Figure 3. Since the density of electrons and ions increases after the evaporation of droplets in APP, the remaining droplets evaporate more quickly as the kinetics of charged particles are enhanced by the evaporation of droplets. This process completes in three steps, i) the electrons coagulate around the droplets heating them to

evaporate after injection, ii) the density of gas mixture increases by the conversion of the liquid phase of droplet into vapour species phase as another species, iii) the rate of ionization is amplified around the remaining droplets, and this process consistently going on until the entire pulse of droplets evaporate into vapour species in the plasma channel. So, this is very important to develop an equilibrium for the evaporation of entire pulses of droplets during the surface coating in order to avoid any perturbing mechanisms, like the saturation and nucleation in APP. From the above understanding, it is evident that the evaporation process is continuously updated by the leading contribution of various ionization mechanisms (PI, DI and SI) that can be authenticated from the temporal profiles of ionization rates from 600 to 700 μsec.

Effect of HMDSO, TEOS and WATER Precursors

In order to distinguish the role of precursor interaction with discharge plasma, a comparison of the electron, vapour species and neutral gas species densities is performed for the following liquid precursors, such as HMDSO, TEOS and water during the positive peak of the discharge current density after 2 ms as shown in Figure 4. These precursors have atypical physical and chemical properties from one another that categorize the significance of interactive performance during the downward fall in APP. The magnitudes of electron (red layer) and vapour species density (green layer) for HMDSO precursor are significantly greater than TEOS and water as depicted in Figure 5 (a - c) because of the intense rate of evaporation and, it is occurring due to the lower surface tension and dynamic viscosity of HMDSO precursor as represented in Table 3. The small radii of liquid droplets are converted quickly into vapours by absorbing sufficient energy from the discharge plasma that further amplifies the neutral gas species density through the phase shifting of precursors. In case of HMDSO liquid precursor, the development of vapour species density (green layer) along the passage of droplets is confined to smaller volume than TEOS and water due to robust rate of evaporation as well as phase shifting of liquid droplets into vapours. This forms a prominent conductive channel in APP and its strength depends on

the rate of evaporation of a particular liquid precursor. It is seen from the numeric values of vapour species density (0.12×10^{-3}, 0.047×10^{-3} and 0.022×10^{-3} g/cm^3) and electron density (~ 4.7×10^{11}, 3.6×10^{11}, 3.2×10^{11} cm^{-3}) that the HMDSO forms a high density channel of conduction than TEOS and water precursors due to the presence of a smaller number of droplets in discharge plasma as shown in Figure 5 (a - c).

Now the development of uniform surface deposition is more probable by applying the volatile liquid precursors in helium discharge plasma, which dissolves rapidly like HMDSO as clearly demonstrated in Figure 5 indicating with different parameters during interaction. For water droplets, this situation does not arise due to the sluggish rate of evaporation. The inert gas species density is increased by absorbing the residue of evaporation that illustrates with slice distributions in the PlasmaStream system for HMDSO, TEOS and water. This means that the number of droplets is greater for TEOS than HMDSO expressing the weak rate of evaporation due to greater surface tension and dynamic viscosity of TEOS. The ionization activities in discharge plasma are dependent heavily on the vaporization of droplets, which can be verified with the values of electron density shifting from HMDSO to water. The chemical formulas for the concerned precursors in Table 3 exhibit that the bonding patterns are different between their atoms and molecules. The rate of evaporation is small for the water droplets due to the existence of hydrogen bonding that have stronger intermolecular forces between their atoms and molecules [32] and ultimately enhance the life time of water droplets as compared to other precursor droplets in APP. These characteristics of water molecules are diversified significantly than other precursors, such as HMDSO and TEOS, which can be confirmed from the three-dimensional modelling outcomes as shown in Figure 5. So, there are greater chances of crashing of higher radii of water droplets on the substrate surface because of smaller rate of evaporation. The density of He-N_2 gas is reduced continuously from HMDSO to water (0.27×10^{-3}, 0.21×10^{-3}, 0.18×10^{-3} g/cm^{-3}), which illustrates with the magnitudes of the slice distributions as presented in Figure 5 (a' - c'). These numerical simulations clearly indicate the

consequences of three distinct precursors for the plasma coating depositions using APP in helium including nitrogen impurities.

Comparison of Fluid-Droplet Model and Experiment

To validate the fluid-droplet modelling results, it is imperative to do a comparison with the experimental observations measured using an additional arrangement of laser diffraction particle size analysis technique with the PlasmaStream atmospheric pressure jet deposition system. We insert a pulse of HMDSO droplets in APP in the size domain (1 μm $\leq r_d \leq$ 6 μm) for the present case. It has been observed from the numerical simulations that the mutual interactions between the droplets, such as grazing and coalescence depend extensively on the initial injection velocity discussed in [33]. The droplets acquire a steady state during the downward displacement in the plasma chamber, but the mutual interactions are very important at higher precursors flow rates (> 100 μL/min). Since the experimental conditions are implemented fully in the fluid-droplet model, the initial injection velocity of droplets in the present simulation case is 1.5×10^3 cm s^{-1}. If the distribution of droplet's pulse is effected by the mutual interaction between them, it certainly modifies the properties of discharge plasma and has strong implications on the deposition of the substrate surface. When the pulse of droplets drifts downward during interaction with discharge plasma, the radii of droplets shrink continuously with the evaporation process shifting the peak of size distribution to the lower domain (2 μm $\leq r_d \leq$ 4 μm). It is evident from the rapid contracting domain of the mean radius of the droplets that the HMDSO precursor is qualified as a fickle because of having smaller values of surface tension, dynamic viscosity and mass density than other liquid precursors, such as TEOS and water.

Figure 6 (a, b) shows better agreement between the size distribution obtained from the fluid-droplet model and the stationary experimental measurements of droplets. This clearly indicates that the

evaporation is the prime mechanism during droplet-plasma interaction for the specific distribution of droplets. Since the laser diffraction imaging lens arrangement has the limiting resolution for the experimental observations of droplets and it can only capture the minimum possible value of radius as 500 nm, but the fluid-droplet model provides the information about the minimum possible size of droplets acquired just before the phase transformation in discharge plasma. The experimental size distributions are recorded in two different experiments under a similar set of working conditions to evaluate the average size distribution of droplets in the plasma chamber. Due to consistent influence of the evaporation process for the pulse of HMDSO precursor, the radii of droplets are shifted into the nanometer range and their typical values lie in the domain (30 nm < $r_d \leq 100$ nm) just before the phase transformation of HMDSO precursor as represented in Figure 6 (a). It is also observed from the numerical simulations that the minimum possible value of droplets is not analogous for different liquid precursors just before the phase transformation in APP, which means that the physical and chemical properties of liquid precursors have tremendous impact during interaction between two-phase flow. The droplets are evaporated into vapour species after accessing sufficient energy for the phase transition that ultimately updates the structure of He-N_2 APP. Consequently, the physical description of complex interaction between the liquid droplets and plasma is characterized by elucidating the spatio-temporal distributions in three-dimensional space that are validated with the experimental and simulation comparison.

Conclusions

We have investigated the spatio-temporal characteristics of droplet-plasma interaction by using a three-dimensional integrated fluid-droplet (FD3d) model using He-N_2 gas mixture. The behavior of evaporation during interaction between two-phase flow has been explored by providing the temporal profiles of droplets that justify the dynamic modification in the structure of APP. Due to the strong

domination of nitrogen impurities, the production of electrons through Penning ionization becomes greater than other ionization mechanisms around the pulse of droplets in the plasma chamber, which is described by the progressive profiles of liquid and plasma parameters. We analyzed the effect of various precursor flow rates (10, 50 and 100 µL/min) of HMDSO in order to contrast the significance of the evaporation process under similar operating conditions. Further, the influence of different precursors is distinguished by exploring the volumetric and slice distributions of electrons, vapour and neutral gas species densities, which show that the rate of evaporation is significantly stronger for HMDSO than TEOS and water precursor droplets in APP. Finally, the fluid-droplet modelling results are validated by comparing with experimental observations to provide the authenticity of numerical modelling results.

Acknowledgments: This work is supported by Science Foundation Ireland under grant 08/SRC/I1411. Special thanks to Dr. Paul Swift for the editing and nice suggestions during the preparation of this manuscript.

References

[1] Rory A. Wolf, Atmospheric Pressure Plasma for Surface Modification, Online ISBN: 9781118547519, Wiley Online Library, **2012**.
[2] U. Kogelschatz, *Plasma Chem. Plasma Process*., **2003**, Vol. 23, no. 1, p. 1.
[3] M. C. Jecklin, G. Gamez, D. Touboul and R. Zenob, *Rapid Commun. Mass Spectrom*, **2008**, 22: 2791–2798.
[4] M. Noeske, J. Degenhardt, S. Strudthoff, U. Lommatzsch, *International J. of Adhesion & Adhesives*, **2004**, 24 171–177.
[5] Laroussi M, *IEEE Trans. Plasma Sci*., **2002**, 30(4) 1409, 1415.
[6] C. Tendero, C. Tixier, P Tristant, J. Desmaison, P. Leprince, *Spectrochimica Acta Part B*, **2006**, 61, 2 – 30.
[7] G. Fridman, A. Shereshevsky, M. M. Jost, A. D. Brooks, A. Fridman, A. Gutsol, V. Vasilets, G. Friedman, *Plasma Chem. and Plasma Process*., April **2007**, Vol. 27, Issue 2, pp 163-176.
[8] K. H. Becker, U. Kogelschatz, K. H. Schoenbach and R. J. Barker, Non-Equilibrium Air Plasmas, Series in Plasma Physics, *IOP Publishing*, Bristol and Philadelphia, ISBN 0 7503 0962 8, **2005**.
[9] Alexander Fridman, Plasma Chemistry, *Cambridge university press*, ISBN-13 978-0-521-84735-3. 83, No. 6, 15 March **1998**.
[10] P. J. O' Rourke, Collective Drop Effects in Vaporizing Liquid Sprays, Ph.D Thesis, 1532-T, *Princeton University*, **1981**.
[11] Park, M., Chang, D., Woo, M., Nam, G., Lee, S., **1998**, *Plasma Exhaust Aftertreatment*, Society of Automotive Engineers, Warrendale, PA.
[12] C. P. Stallard, M. M. Iqbal, M. M. Turner, D. P. Dowling, *Plasma Processes and Polys*., October **2013**, Vol. 10, Issue 10, pp. 888–903.
[13] A. A. Amsden, KIVA-3V: A Block-Structured KIVA Program for Engines with Vertical or Canted Valves, July **1997**, LA-13313-MS, UC-1412, Los Alamos, New Mexico 87545.
[14] Y. Shan and J. Mostaghimi, *Spectrochimica Acta Part B*, **2003**, 58 1959 - 1977.
[15] M. Meyyappan, Computational Modelling in semiconductor processing, Artech House, ISBN-0 89006-707-4, **1995**.

[16] William A. Sirignano, University of California, Irvine, *Cambridge University Press*, ISBN-13 978-0-521-63036-8 hardback, **1999**.
[17] C. C. Leiby, JR. and H. J. Oskam, *Physics of fluids*, September **1967**, Vol. 10, No. 9.
[18] M. M. Iqbal, M. M. Turner, Proceeding in *63rd Annual GEC and 7th ICRP*, **2010**, Volume 55, Number 7, October 4 - 8, Paris, France.
[19] P. Anthony, F. Herbert, L. O'Neill, J. Jaroszynska-Wolinska, C. Stallard, Amsarani Ramamoorthy, D. P. Dowling, *Plasma Process. Polym*., **2011**, 8, 230-238.
[20] N. Ashgriz, J. Y. Poo, *J. Fluid Mechanics*, **1990**, 221 183.
[21] Francis H. Harlow and Anthony A. Amsden, J. of Computational phys., **1971**, 8, 197-213.
[22] M. M. Iqbal, M. M. Turner, Contrib. to Plasma Phys., **2014**, ctpp.201400002, Issue 9, Vol. 54.
[23] G. J. M. Hagelaar, Ph.D Thesis, *Technische Universiteit Eindhoven*, **2000**.
[24] D. W. Peaceman and H. H. Rachford, JR., J. Soc. Indust. Appl. Math., March **1955**, Vol. 3, No. 1.
[25] Stephen L. Adler, *Physical Rev*., **1981**, 23, No. 12.
[26] D. P. Lymberopoulos and D. J. Economou, *J. Vac. Sci. Technol*. A, **2012**, 12(4), 1994, pp. 1229 - 1236.
[27] Wolfram|Alpha: Wolfram Alpha LLC.
[28] G. J. M. Hagelaar, G. M. W. Kroesen, U. van Slooten, and H. Schreuders, J. Appl. Phys., **1999,** 88, No. 5, 2252.
[29] L. L. Alves, G. Gousset and C. Ferreira, *Phys. Rev. E*, **1997**, 55 (1), p. 890.
[30] X. Yuan and L.L. Raja, *IEEE Trans. on Plasma Sci*., **2003**, Vol. 31, No: 4, pp. 495 - 503.
[31] G. Hagelaar, L. Pitchford, *Plasma Sources Sci. Technol*., **2005**, 14, 722.
[32] Ralph H. Petrucci, F. Geoffrey Herring, Jeffry D. Madura, Carey Bissonnette, General Chemistry: Principles and Modern Applications, Upper Saddle River: Pearson/Prentice Hall, **2007**.
[33] M. M. Iqbal, M. M. Turner, "Behavior of HMDSO Liquid Precursor Droplets in APD Plasma and Gas Mixture", Proceeding in *31st ICPIG*, **2013**, July 14 -19, Granada, Spain.

Figure. 1. (a) Symbolic representation of PlasmaStream^{TM} atmospheric plasma jet deposition system with Laser source [12] and (b) Simplified geometry for three dimensional fluid-droplet model.

Figure 2. Temporal evolution of (a) mean radius, (b) mean temperature, (c) mean axial velocity and (d) mean vapour species density for the entire pulse of water droplets at flow rate = 10 µL/min, gas flow rate = 5 L/min, f = 20 kHz and V_0 = -13.5 kV.

Figure 3. Spatial distribution of vapour species density under particular HMDSO precursor flow rates (10, 50 and 100 µL/min) in He-N_2 APP at gas flow rate = 5 L/min, f = 20 kHz and V_0 = -13.5 kV.

Figure 4. Temporal evolution of rates for the Direct ionization, Penning ionization and Stepwise ionization around the pulse of droplets using HMDSO precursor droplets at flow rate = 100 µL/min and gas flow rate = 5 L/min, V_0 = -13.5 kV in He-N_2 and He-Air gas mixtures.

Figure 5. Volumetric spatial profiles of vapour species and electron density, and slice distribution of neutral gas species density for different precursors (a, a') HMDSO, (b, b') TEOS and (c, c') water at precursor flow rate = 100 µL/min, gas flow rate = 5 L/min, f = 20 kHz and V_0 = -13.5 kV.

Figure 6. Droplet size distributions for HMDSO liquid droplets using (a) Fluid-droplet model and (b) Experimental measurements in He-N_2 APP at precursor flow rate = 100 µL/min, gas flow rate = 5 L/min, f = 20 kHz and V_0 = -13.5 kV.

Table 1. Input initial parameters for the Fluid-Droplet Model

Fluid-droplet model variables	**Initial input values**
Density of quasi-neutral plasma at t = 0.0	1.0×10^{9} cm^{-3}
Axial length and diameter of chamber	75 mm and 15 mm
External imposed potential (V_0)	-13.5 kV
Driving frequency (f)	20 kHz
Operating pressure (p)	760 torr
Gas temperature (T_g)	300 K
Precursor droplet temperature (T_d)	292 K
Injection droplet velocities (u_r, u_z and u_θ)	(1.5×10^{3}, 1.0×10^{-3} and 1.0×10^{-3}) cm s^{-1}
Gas species density (ρ_g)	0.1617×10^{-3} g cm^{-3}
Vapour species mass fraction (Y)	0.01
Swirl velocity (w) of gas	1.0×10^{-3} cm s^{-1}
Diffusivity of helium gas	1.6313 cm^2 s^{-1}
Angular rotation (θ)	0.1 radians
Time steps for droplets (Δt_1) and plasma (Δt_2)	0.1×10^{-5} s and 2.0×10^{-9} s
Initial energy of electrons and ions	0.5 eV and 0.026 eV

Table 2. Initial and boundary conditions for Fluid-Droplet Model

Inlet (z = 0)	**Centerline (r = 0)**	**Angular axis ($\theta = \theta$)**
$u = Q_1/\pi(r_2^2 - r_1^2)$ for $r_1 < r \le r_2$	$v = 0, w = 0$	$v = 0, w = 0$
$u = 0$ for $r_2 < r \le r_3$	$\partial h/\partial r = 0$	$\partial h/\partial\theta = 0$
$u = Q_2/\pi(R_0^2 - r_3^2)$ for for $r_3 < r \le R_0$	$\partial Y/\partial r = 0$	$\partial Y/\partial\theta = 0$
$v = 0, w =$ User's choice, $Y = 0$	$\partial u/\partial r = 0$	$\partial(\rho_g u)/\partial\theta = 0$
$V = V_0 \sin(2\pi ft)$ for $r_2 < r \le r_3$	$\partial V/\partial r = 0$	$\partial V/\partial\theta = 0$
Exit ($z = L$)	**Glass wall ($z = R_0$)**	**Angular axis ($\theta = \theta_0$)**
$\partial(\rho_g u)/\partial z = 0$	$v = 0, w = 0$	$v = 0, w = 0$
$\partial h/\partial z = 0$	$\partial h/\partial r = 0$	$\partial h/\partial\theta = 0$
$\partial Y/\partial z = 0$	$\partial Y/\partial r = 0$	$\partial Y/\partial\theta = 0$
$\partial v/\partial z = 0, \partial w/\partial z = 0$	$u = 0$	$\partial(\rho_g u)/\partial\theta = 0$
$V =$ Grounded	$\partial V/\partial r = 0$	$\partial V/\partial\theta = 0$

Table 3. Parameters used in Fluid-droplet model

Liquid Precursors	Surface tension × 10^{-2} (N cm^{-1})	Dynamic viscosity (Pa s)	Boiling point (K)	Mass Density (10^{-3} × g cm^{-3})
Water (H_2O)	7.197	8.9×10^{-4}	373.15	1000.0
TEOS ($C_8H_{20}O_4Si$)	2.280	7.9×10^{-1}	441.15	934.0

HMDSO($C_6H_{18}OSi_2$)	1.531	4.8×10^{-4}	374.00	758.4

Table 4: Variables in Fluid-Droplet Model (FD3d)

Symbols	Physical Description
ρ_g, $\vec{u}$, P, Γ_μ, k, $\vec{j}$, $\vec{E}$, h, D_{AB}, Y and S	Represent the gas density, velocity of gas, pressure, momentum, thermal conductivity, joule heating, electric field, enthalpy, diffusion coefficient, vapour species mass fraction and various source terms in the set of Eqs. (1 - 4).
C_p	Specific heat at constant pressure
$\vec{x}_p$	Position of droplets in parcels
$\vec{u}_p$	Velocity of droplets in parcels
$\vec{u}'$	Velocity of gas with fluctuations
ρ_l	Density of liquid precursors
k_B	Boltzmann constant
g	Gravitational constant
R	Universal gas constant
$c_D = (24/R_e)(+R_e^{2/3}/6)$	c_D is used in the calculation of drag coefficient
$R_e = (\rho_g\lvert\vec{u}+\vec{u}'-\vec{u}_d\rvert r_d)/\mu_g(\bar{T}_g)$	Reynolds number of droplets
$\vec{F} = K_p(+\vec{u}'-\vec{u}_d) - (1/\rho_l)\vec{\nabla}p + g\hat{k}$	Forces acting on the droplets
$\mu_g(\bar{T}_g)$	Viscosity of gas
$\bar{T}_g = (T_g + 2T_d)/3$	$\bar{T}_g$ and T_g are the average and local gas temperatures
$Nu_{(g,\,l)}$	Nusselt number of gas and liquid
Y_{V_s}, Y_V	Liquid vapour mass fraction of the surface of the droplet and inside APP
λ_g	Heat conductivity of gas
$\mathrm{Pr} = \mu_g c_{pg} / \lambda_g$	Gas-phase Prandtl number
c_{pg}, c_l	Specific heat of gas and liquid at constant pressure
T_s	Surface temperature of droplet
$P_g = \rho_g R T_g (Y_v / W_v + Y_I / W_I)$	Equation of state
$h_g = (c_{pv} Y_v + c_{pI} Y_I)\, T_g = c_{pg} T_g$	Equation of state
W_V, W_I	Molecular weight of liquid vapours and gas

c_{p_v}, c_{p_l}	Specific heat of vapour species and inert gas species at constant pressure
$h_l(T_d) = C_{pv}\, T_d - L(T_d)$	Enthalpy of liquid droplets
S, S_M and S_E	Source terms of the mass transfer, momentum transfer and gas enthalpy, and details presented in [10]
$f'(r_d) = (1/\bar{r}_d)\exp(-r_d/\bar{r}_d)$	X-squared distribution function, r_d and $\bar{r}_d$ are the radius and number-averaged droplet radius for initial distribution
μ_p, T_p and q_p	Mobility, temperature and charge for discharge species of plasma
Arc length (s_θ)	$r\theta$, where r is the radius and θ is the angle

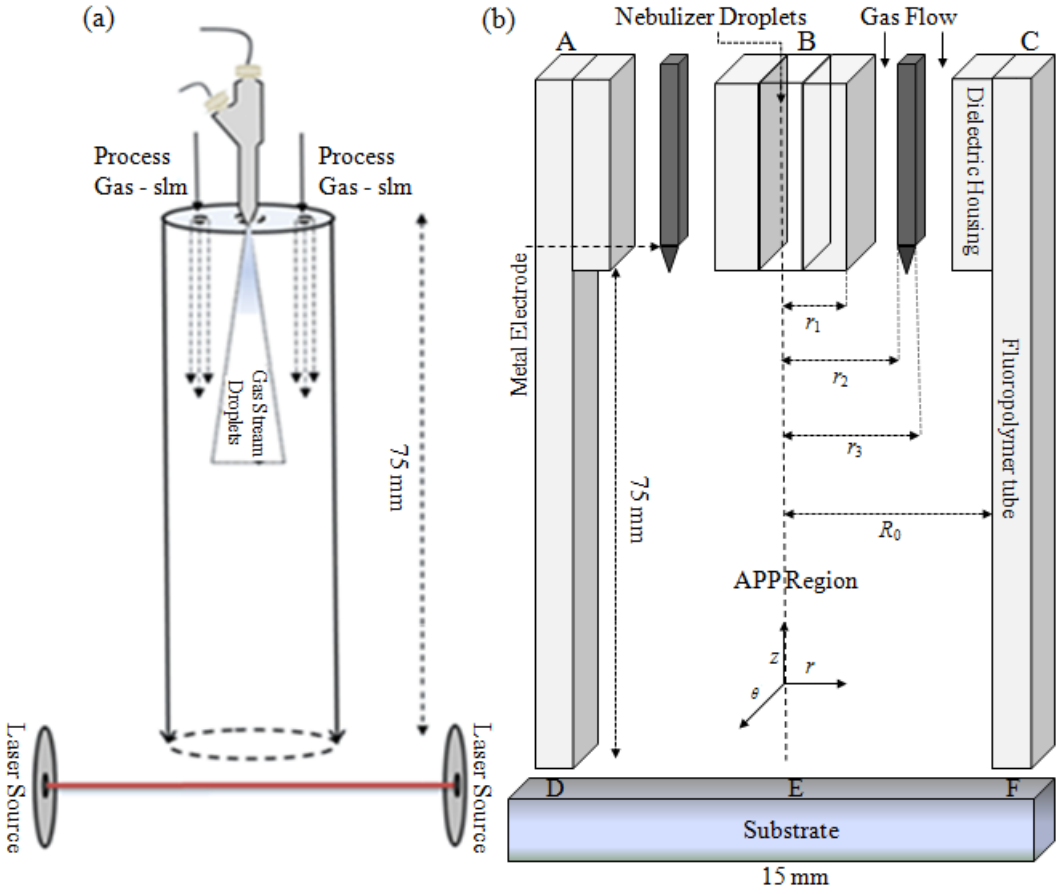

Figure 1

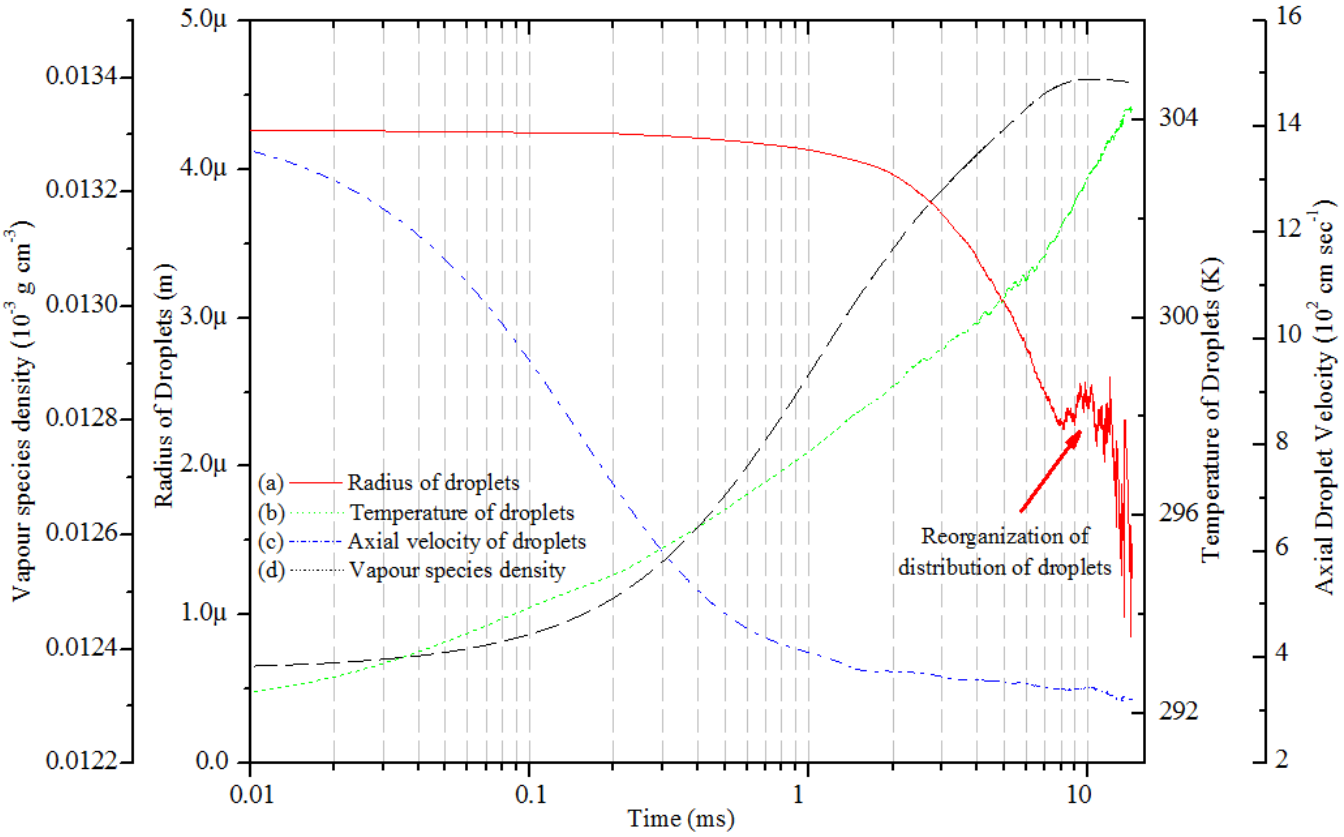

Figure 2

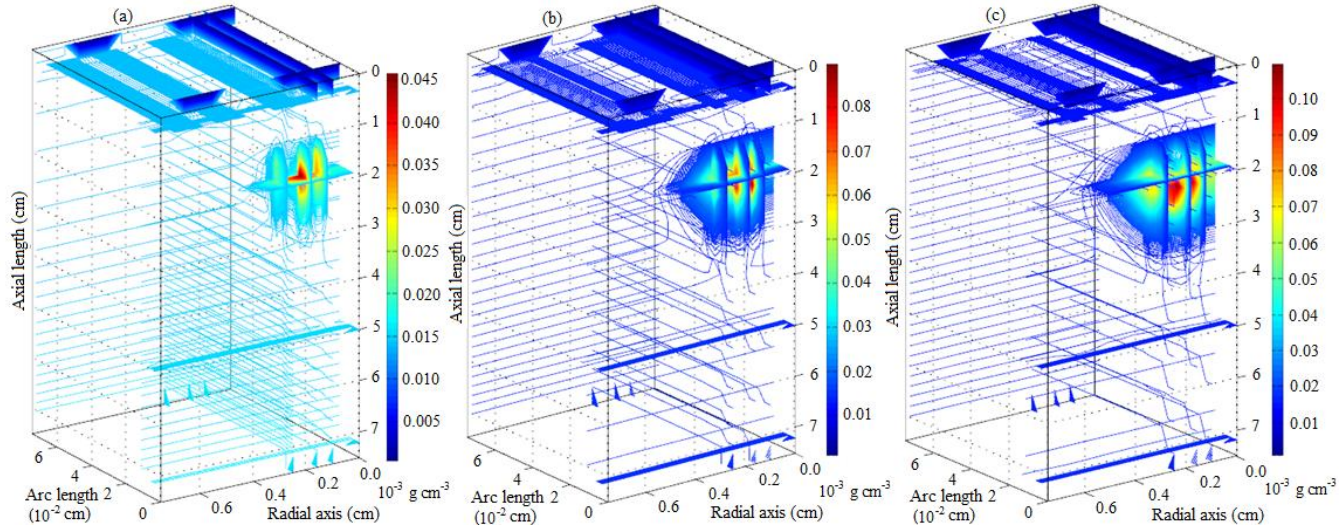

Figure 3

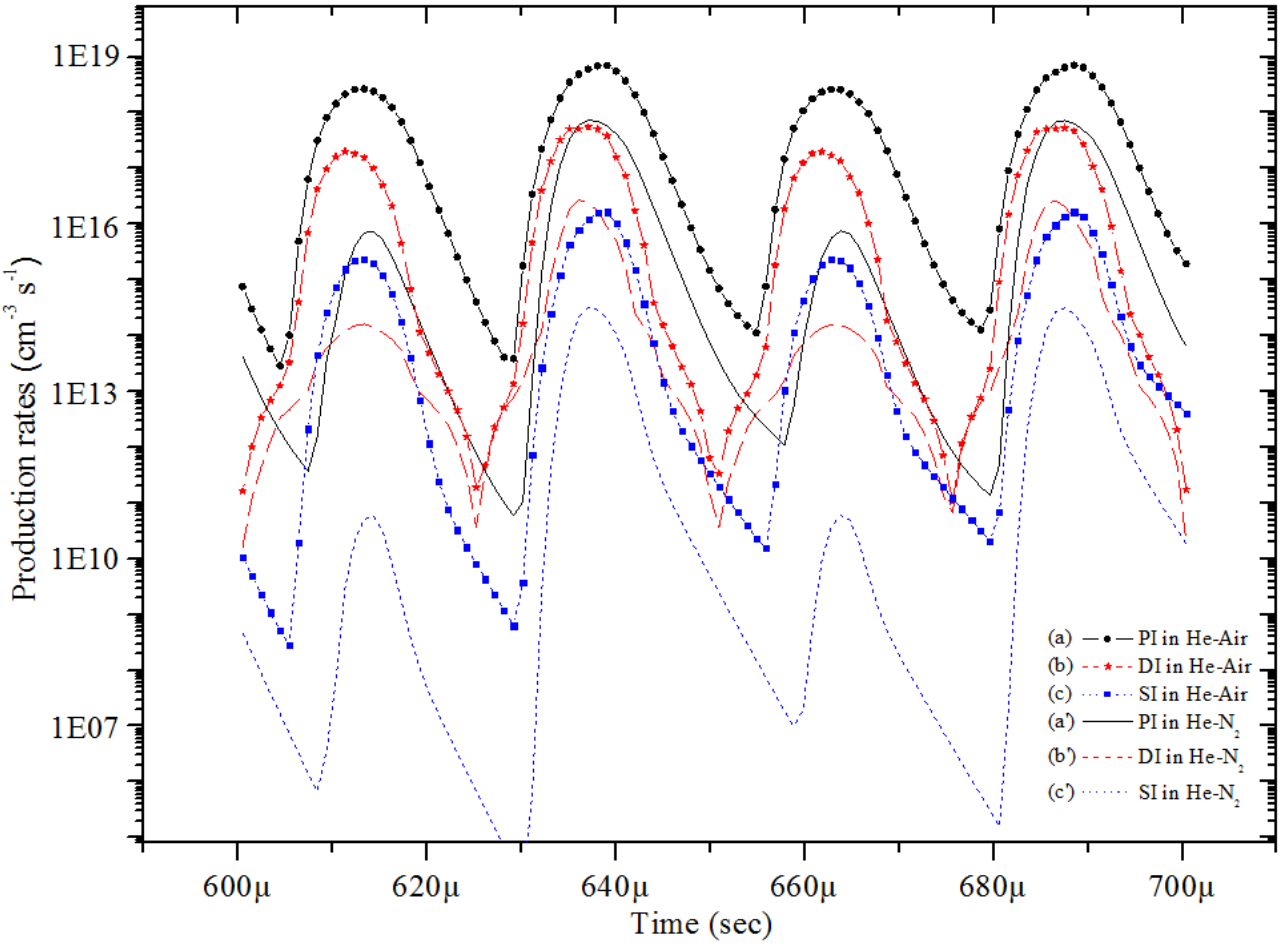
1E19
1E16
1E13
1E10
1E07
Production rates (cm^{-3} s^{-1})
600µ
620µ
640µ
660µ
680µ
700µ
Time (sec)
(a) PI in He-Air
(b) DI in He-Air
(c) SI in He-Air
(a') PI in He-N$_2$
(b') DI in He-N$_2$
(c') SI in He-N$_2$

Figure 4

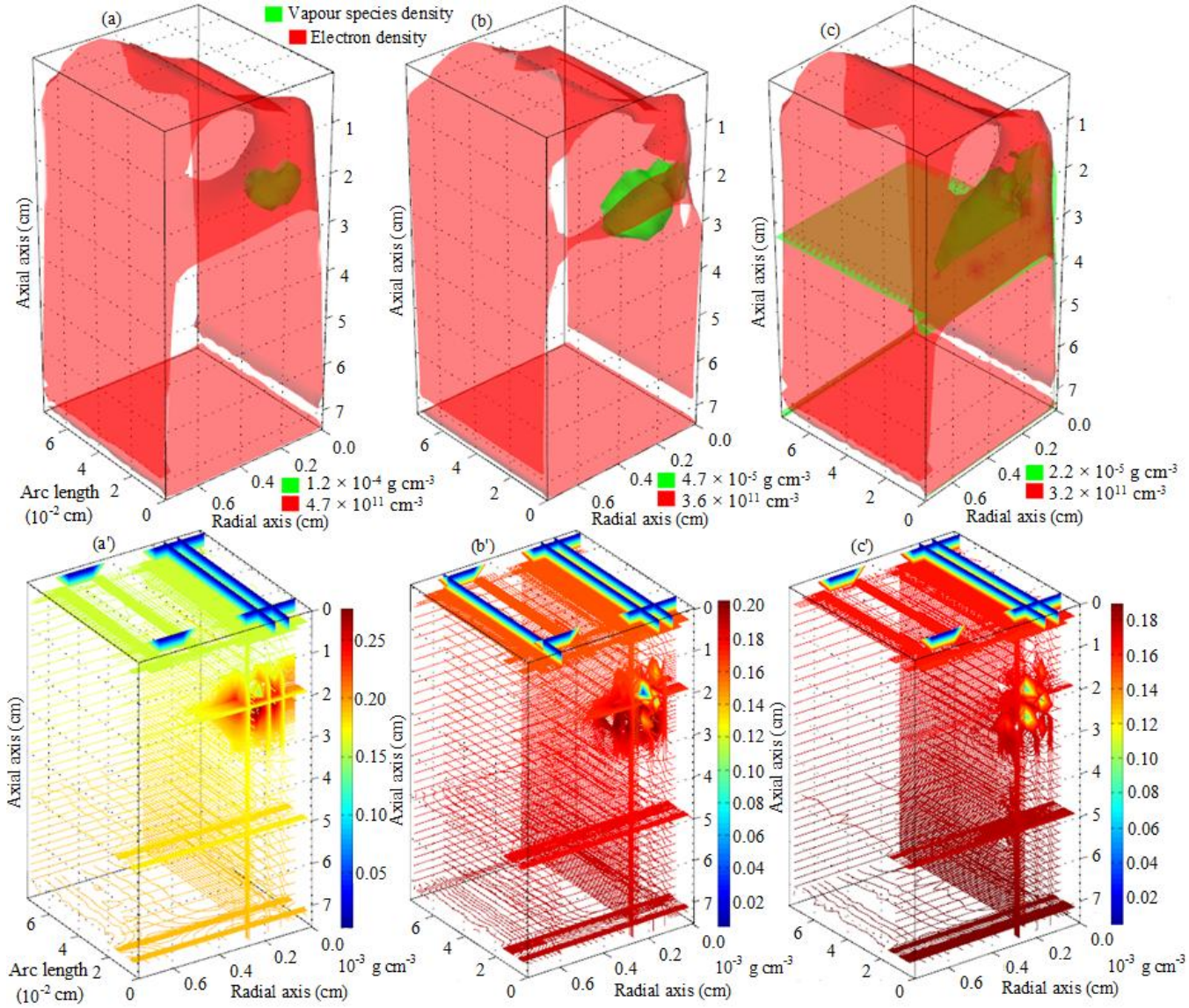
(a)
Vapour species density
Electron density
(b)
(c)
Axial axis (cm)
Arc length
(10^{-2} cm)
Radial axis (cm)
1.2×10^{-4} g cm^{-3}
4.7×10^{11} cm^{-3}
4.7×10^{-5} g cm^{-3}
3.6×10^{11} cm^{-3}
2.2×10^{-5} g cm^{-3}
3.2×10^{11} cm^{-3}
(a')
(b')
(c')
10^{-3} g cm^{-3}

Figure 5

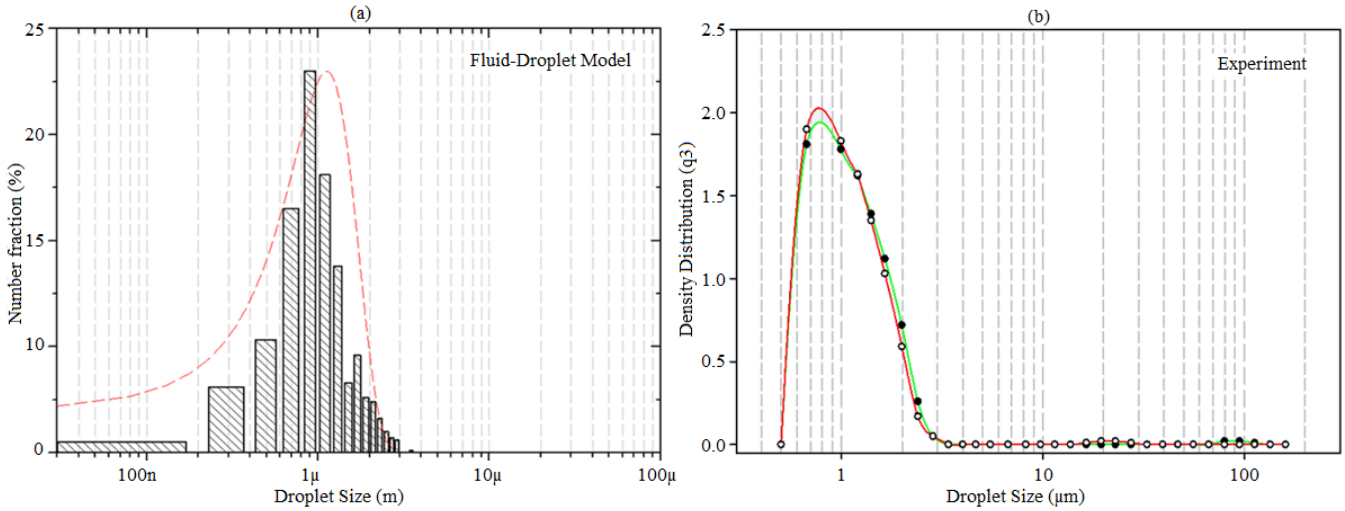
(a)
Fluid-Droplet Model
Number fraction (%)
25
20
15
10
0
100n
1µ
10µ
100µ
Droplet Size (m)
(b)
Experiment
Density Distribution (q3)
2.5
2.0
1.5
1.0
0.5
0.0
1
10
100
Droplet Size (µm)

Figure 6